Engineering 59 (2026) 352–363

Contents lists available at ScienceDirect

Engineering

journal homepage: www.elsevier.com/locate/eng

Research
Wireless Communications—Article

A Dual-Broadband Liquid-Crystal Programmable Metasurface and Its Application in Terahertz Wireless Communications

Yuan Fu [a,#], Yuanbo Li [b,#], Xiaojian Fu [a,*], Lu Xu [c], Yujie Liu [a], Qun Yan Zhou [a], Jun Yang [c], Chong Han [b,*], Jun Yan Dai [a], Qiang Cheng [a], Tie Jun Cui [a,*]

[a] State Key Laboratory of Millimeter Waves, Southeast University, Nanjing 210096, China
[b] Terahertz Wireless Communications (TWC) Laboratory, Shanghai Jiao Tong University, Shanghai 200240, China
[c] National Engineering Laboratory of Special Display Technology, Academy of Opto-Electric Technology, Hefei University of Technology, Hefei 230009, China

ARTICLE INFO

Article history:
Received 13 February 2025
Revised 29 July 2025
Accepted 1 August 2025
Available online 9 September 2025

Keywords:
Programmable metasurface
Terahertz communication
Reconfigurable intelligent surface
Dual-frequency
Broadband
Beamforming

ABSTRACT

Terahertz communication technology is envisioned as a promising candidate for the pivotal spectrum technology in future wireless communication networks. However, the limited penetration ability of terahertz waves makes line-of-sight (LoS) transmission indispensable, hindering the extensive application of terahertz communications. In this work, a novel liquid-crystal programmable metasurface (LCPM) is proposed for the first time, which can effectively achieve dual-broadband beam manipulation to improve link stability and extend coverage for terahertz communications in non-line-of-sight (NLoS) scenarios. The LCPM is operated in both the W band that covers 94 GHz and the D band that covers 140 GHz, corresponding to *x*-polarized and *y*-polarized wave incidence, respectively. Based on the proposed LCPM, realistic NLoS terahertz communication links are established and showcased. Communication measurements substantiate that the LCPM is capable of realizing extensive dynamic channel regulations and long-distance communications across both bands in various modulation schemes, supporting real-time high-speed video transmission. The experimental results validate the feasibility of employing the LCPM for terahertz wireless communications, paving the way for developing and implementing ubiquitous terahertz communication networks even with LoS blockage.

1. Introduction

Terahertz wireless communication, which leverages the vast spectrum resources in the 0.1–10.0 THz band, is anticipated to be a crucial enabling technology for next-generation wireless communication networks [1–4]. The expansive consecutive bandwidth in the terahertz band facilitates ultra-high data rates, ultra-low transmission delays, and ultra-high positioning accuracy, thus supporting intelligent applications such as virtual reality, augmented reality, and autonomous driving [5–8]. Nevertheless, as the operational frequency increases, there is a rapid escalation in the propagation loss of electromagnetic waves in free space, which increases quadratically with the frequency, as defined by the Friis transmission equation. Apart from the severe propagation loss, significant diffraction and penetration losses make terahertz wireless communications more vulnerable when the line-of-sight (LoS) wireless link is obstructed [9,10]. This limitation results in weak coverage and communication stability in non-line-of-sight (NLoS) scenarios, which hinders the development of terahertz wireless communication networks, especially for long-range coverage. To build reliable terahertz communication networks, such challenges must be addressed.

To deal with LoS blockage and extend terahertz coverage in NLoS scenarios, one straightforward approach is to deploy more access points or active relays in the network, in order to cover more areas with direct LoS propagation. However, this method significantly increases hardware costs and energy consumption, and may result in substantial interference issues that could degrade the overall performance of the network. An energy-efficient alternative is to employ a passive reflecting surface (PRS) to create a strong reflected path from the transmitter (Tx) to the receiver

* Corresponding authors.
E-mail addresses: fuxj@seu.edu.cn (X. Fu), chong.han@sjtu.edu.cn (C. Han), tjcui@seu.edu.cn (T.J. Cui).
The authors contribute equally to this work.

https://doi.org/10.1016/j.eng.2025.08.040

(Rx) [11–13]. For instance, metallic surfaces can function as electromagnetic mirrors capable of reflecting electromagnetic waves with nearly no reflecting loss, thereby creating a virtual LoS path. Nevertheless, the relationship between the incidence angle and emergence angle determined by Snell's law makes the NLoS propagation path fixed, unable to meet the ubiquitous communication demand in NLoS scenarios.

In contrast to a rigid PRS, a superior solution is to implement a reconfigurable intelligent surface (RIS) that can actively reconstruct the wireless environment by switching coding patterns, thereby realizing signal quality enhancement, dynamic channel regulation, and coverage extension [14–17]. The realization of RIS is contingent upon the utilization of programmable metasurfaces, which have gained considerable research interest over the past decade owing to their unprecedented electromagnetic manipulation capabilities and broad application prospects. By strategically designing and configuring meta-atoms, a metasurface can be created that can control the amplitude, phase, polarization, frequency, and orbital angular momentum of electromagnetic waves, enabling diverse functionalities such as radar cross-section (RCS) reduction [18], abnormal beam deflection [19,20], polarization conversion [21], holographic imaging [22], non-reciprocal transmission [23], nonlinear harmonic generation [24,25], and vortex beam generation [26]. Typically, semiconductor components (e.g., positive–intrinsic–negative (PIN) diodes [27], varactors [28], high-electron mobility transistor (HEMT) [29], and application-specific integrated circuits (ASICs) [30]), tunable materials (e.g., liquid crystals (LCs) [31–34] and graphene [35]), and phase change materials (e.g., vanadium dioxide (VO_2) [36], and $Ge_2Sb_2Te_5$ (GST) [37]) have been incorporated into meta-atoms, enabling dynamic adjustment of the electromagnetic responses of the meta-atoms to achieve programmable metasurfaces. However, considering the working frequency and corresponding size of a meta-atom, the realization of terahertz programmable metasurfaces based on a semiconductor process will be generally challenging and costly. Programmable metasurfaces based on graphene and phase change materials still have limitations in achieving pixelated control.

Notably, LC-based programmable metasurfaces have garnered significant attention for their large phase-tuning range, scalability in large-scale array manufacturing, low cost, and low power consumption. Recently, a variety of programmable metasurfaces operating in the millimeter wave and terahertz frequency and employing a metal–LC–metal sandwich structure have been proposed. Wu et al. [38] reported a programmable metasurface operating at 0.672 THz that achieves one-dimensional (1D) beam scanning with a maximum range of 32°. Fu et al. [39] demonstrated a terahertz programmable metasurface capable of beam steering across a range of ±60° at 0.645 THz. Additionally, advancements in two-dimensional (2D) programmable metasurfaces have recently emerged. Li et al. [40] presented a large-scale 2D programmable metasurface operating on the principle of modulo-addition that facilitates the flexible control of terahertz waves in the upper half-space. Wang et al. [41] engineered an individually addressable transmissive programmable metasurface that proficiently enables terahertz near-field manipulations and the generation of Bessel beams. These studies have significantly improved the ability of programmable metasurfaces to manipulate terahertz waves with increased flexibility.

As metasurface techniques continue to evolve, there is increasing interest in assessing the performance of RISs in aiding wireless networks. Given advancements in design and fabrication methods, numerous studies have been conducted on RIS evaluations in the microwave and millimeter-wave bands [42–47]. For instance, Malik et al. [42] implemented a 32×32 prototype of a reflectarray metasurface under different scenarios at 28 and 38 GHz. The experimental results showed that the signal enhancement from using an RIS reached 20–25 dB in the tested bands. Moreover, Shah et al. [43] presented an experimental analysis of an RIS-enabled indoor localization scheme at 3.75 GHz. The experiment findings demonstrated that the indoor localization accuracy was greatly improved by incorporating an RIS, achieving an impressive success rate of 82.4%. However, comprehensive experimental studies on RIS-aided terahertz communications have not yet been reported, and the majority of existing works that involve terahertz RISs are primarily based on simulations. For example, Huo et al. [48] proposed a distributed RIS framework that was demonstrated to be effective in overcoming the mobile human blocking issue, improving terahertz signal coverage, and increasing signal-to-noise ratios (SNRs) and quality of service (QoS). Based on a multi-hop RIS framework, Huang et al. [49] proposed a novel hybrid beamforming design to improve the 50% coverage range of terahertz communications compared with benchmarks. Additionally, utilizing a stacked RIS architecture, An et al. [50,51] put forward a simplified multiple-input multiple-output (MIMO) transceiver design scheme and a direction-of-arrival (DOA) estimation method, which hold potential to realize a low-complexity integrated sensing and communications (ISAC) terahertz network. To summarize, broadband RIS design and practical RIS-aided link performance evaluation in the terahertz band remain unexplored.

Herein, we propose a novel liquid-crystal programmable metasurface (LCPM), which is capable of assisting dual-broadband terahertz wireless communications. Based on a carefully designed anisotropic meta-atom, the LCPM can function in two separate frequency bands under the excitation of orthogonally polarized waves, corresponding to the W band covering 94 GHz with the *x*-polarized wave and the D band covering 140 GHz with the *y*-polarized wave. The LCPM's capabilities of flexible beam manipulations, encompassing dual beam steering, single-beam scanning, and dual-band independent beam control, are confirmed through both numerical simulations and experiments, providing a solid foundation to enhance wireless communications. Leveraging its powerful beam-manipulation abilities, the LCPM successfully establishes and dynamically regulates a wireless channel in three-dimensional (3D) space, enabling a flexible and high-quality link connection between the Tx and Rx under quadrature phase-shift keying (QPSK) modulation in an NLoS transmission scenario, compared with no LCPM or the deployment of only a PRS. To further improve the transmission efficiency over the terahertz channel, higher-order modulation schemes, including 16-quadrature amplitude modulation (QAM) and 64-QAM, are verified in the dual-band range with long-distance propagation.

Finally, as a showcase of terahertz communications, we provide an experimental demonstration of real-time high-speed video transmission. The excellent performance of the proposed LCPM in assisting terahertz wireless communication demonstrates the LCPM as an effective solution for advancing the ubiquitous terahertz communication networks.

2. Design of a dual-broadband LCPM

Fig. 1 depicts a schematic diagram of the architecture for LCPM-aided terahertz wireless communications. In the exemplary scenarios, terahertz wireless signals are transmitted from the base station to the users. However, the wireless channel might be blocked by various obstacles such as bookshelves, buildings, or humans, hindering the effective establishment of wireless communications. To address this issue, the LCPM is deployed to actively regulate the wireless electromagnetic environment and re-establish a stable communication link between the base station and users, thereby ensuring wireless data transmissions. Specifically, when users are positioned at various locations, the

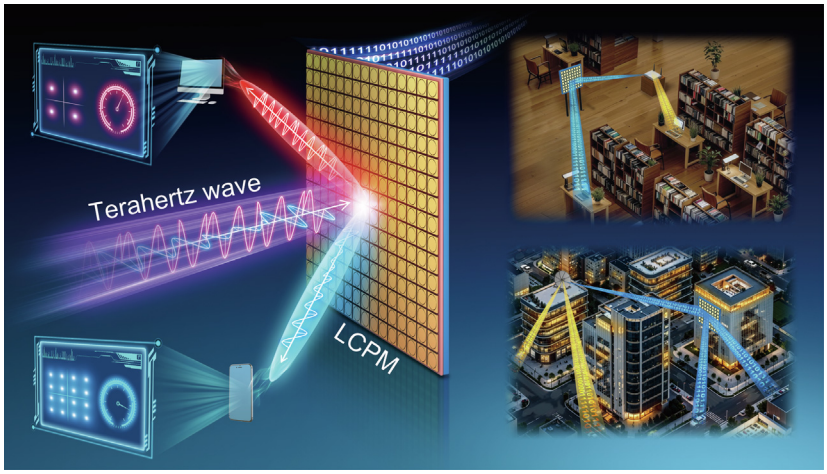

Fig. 1. Schematic diagram of the LCPM assisted dual-broadband terahertz wireless communications. The baseband signals carrying information are transmitted after terahertz carrier modulation with different polarizations and frequencies. When terahertz waves interact with the LCPM, electromagnetic waves of different polarizations and frequencies are reflected to the corresponding Rx to establish an efficient channel link connection, utilizing the programmability of the LCPM. In these illustrations, possible use cases of LCPM are shown. The wireless data from a base station or Tx cannot be transmitted to the client or target user through an LoS link due to obstacles. By reasonably deploying the LCPM, the LoS link can be re-established to complete high-speed data transmission.

corresponding azimuth and elevation angles can be extracted and subsequently mapped to the coding pattern of the metasurface, which is then sent to the digital-to-analog converter (DAC) control module in the form of a bit stream. A corresponding coding pattern update is then accomplished by converting the bit stream into a voltage distribution, thereby establishing an effective wireless link. Thanks to its well-designed element geometry, the LCPM is capable of respectively manipulating the *x*-polarized and *y*-polarized waves at different operating frequencies, enabling dual-frequency and dual-polarized programmability. Furthermore, by exploiting the 2D programmable features of the LCPM, customized wireless links can be independently established under wave incidences with different polarization and frequencies, thereby supporting dual-band and high-speed terahertz wireless data transmissions simultaneously.

2.1. Design of the LCPM meta-atom

Figs. 2(a) and (b) illustrate the anisotropic structure of the proposed dual-broadband meta-atom, along with the simulated amplitude and phase response curves for different polarized incidence waves. As shown in Fig. 2(a), the meta-atom is designed by etching two semi-toroidal slots of width R–r into a gold patch (where R and r are the outer radius and inner radius of the semi-toroidal slot, respectively); this achieves the specific frequency responses for the *x*-polarized and *y*-polarized waves, respectively, while maintaining high reflectivity. In addition, the large metal area design contributes to the establishment of a more uniform electric field between the upper and lower metal patches, thereby enabling robust control of the interlayer LC molecules. Following meticulous optimization, the designed meta-atom can cover 94 GHz for *x*-polarized incidence and 140 GHz for *y*-polarized incidence, both of which fall within the communication window bands. The simulated amplitude and phase response curves for different polarized incidence waves are depicted in Fig. 2(b). Under the condition of *x*-polarized incidence, the meta-atom is resonant near 100 GHz when the dielectric constant of the LC is 2.55, corresponding to the pre-orientation state of the LC molecules. When the dielectric constant is adjusted to 3.65, indicating the complete deflection state of the LC molecules, the resonant point of the meta-atom shifts to approximately 90 GHz, leading to a corresponding change in the phase curve. In the above two states, the phase difference is observed within 180° ± 20° in the range of 92.7–97.8 GHz, and a 1-bit coding can be defined. Similarly, the 1-bit phase coding condition can be realized in the 130.0–140.6 GHz band under the *y*-polarized wave incidence.

Figs. 2(c) and (d) present the measured amplitude and phase responses of the metasurface under *x*-polarized and *y*-polarized wave excitation, respectively. For the *x*-polarized wave, as the external square wave voltage increases from 0 to 5 V, the resonant frequency of the metasurface shifts from 112.5 to 101.6 GHz, accompanied by a corresponding change in phase difference. The metasurface exhibits a phase difference within 180° ± 20° in the 104–110 GHz range. It should be noted that the measured operating frequency band deviates from the design value. This discrepancy may be attributed to the errors that occurred during fabrication and assembly, especially concerning the low flatness of the pixelated control circuit, which was manufactured using the multi-layer printed circuit board (PCB) process. This issue results in inaccurate thickness of the LC between the upper and lower metal patches, significantly influencing the resonant frequency of the meta-atom under *x*-polarized wave incidence. A potential solution is to apply LC-on-silicon (LCoS) technology, which has better fabrication flatness and greater processing accuracy [52,53]. The 180° ± 20° phase difference for the *y*-polarized wave is satisfied within the frequency range of 131.0–139.8 GHz, which agrees well with the simulated result. It should be noted that measurements above 140 GHz were not conducted, due to instrument limitations. The metasurface array designed in this study comprises a total of 50 × 50 meta-atoms, among which every set of 2 × 2 meta-atoms is independently controlled as a super-element. Thus, there are 25 × 25 controllable super-elements. The detailed measurement method about amplitude and phase response of the LCPM is provided in Appendix A Section S1.

2.2. Dual-broadband beam manipulation

According to the generalized Snell's law, the reflection angle of a normally incident plane wave on an interface with a discontinuous phase distribution, such as a metasurface, can be determined as follows:

$$\theta = \sin^{-1}\left(\frac{\lambda_0}{\Gamma}\right) \tag{1}$$

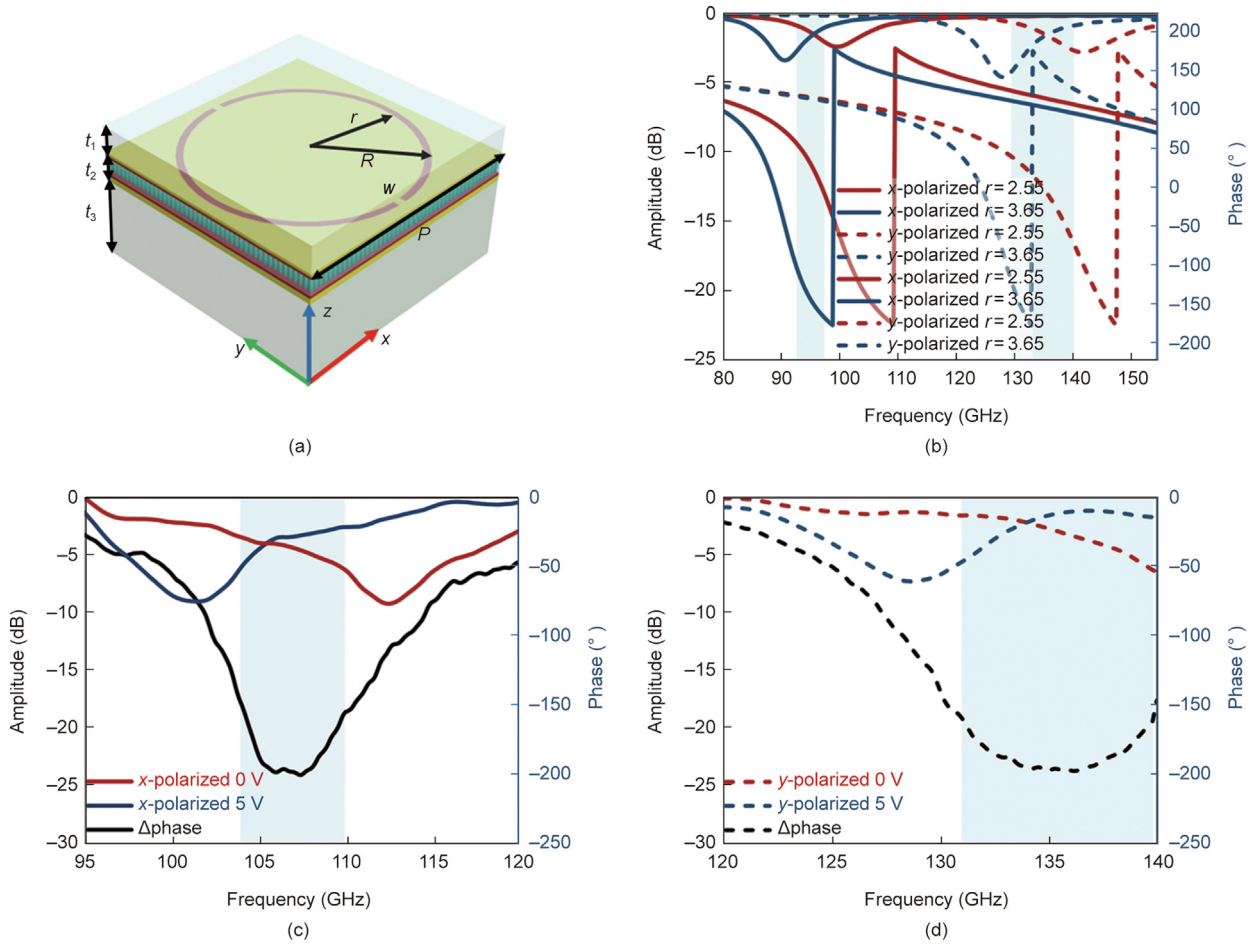

Fig. 2. The proposed dual-broadband meta-atom and its corresponding amplitude and phase curves under different polarized wave incidences. (a) Structure of the designed meta-atom, where the period of the meta-atom P = 900 μm, the outer radius of the semi-toroidal slot R = 415 μm, the inner radius of the semi-toroidal slot r = 385 μm, the thickness of quartz t_1 = 200 μm, the thickness of LC t_2 = 60 μm, the thickness of PCB t_3 = 1600 μm, and the retained metal width w = 30 μm. (b) Simulated amplitude and phase response curves for *x*-polarized and *y*-polarized incident waves with different LC dielectric constants. (c, d) The measured amplitude and phase response curves under different biased voltages for both (c) *x*-polarized and (d) *y*-polarized incident waves.

where Γ represents the phase gradient period of the metasurface, λ_0 is the working wavelength of the electromagnetic wave in a vacuum, and θ is the elevation angle. Based on Eq. (1), the reflection angles of the metasurface under varying coding patterns and different incident polarizations can be calculated. For the coding pattern illustrated in Fig. 3(a), corresponding to Γ = 3600 μm, the calculated beam-deflection angle at the optimal frequency of 95.5 GHz is about ±60.8°, and the simulated value is approximately ±60.0° under *x*-polarized wave incidence, as shown in Fig. 3(b). The calculated abnormal reflection angle at the optimal frequency of 134 GHz is around ±38.5°, and the simulated result is about ±38.2° under *y*-polarized wave incidence, as presented in Fig. 3(c), which is highly consistent with the theoretical calculation. More results about dual beam scanning are provided in Appendix A Section S2.

Furthermore, independent control of the abnormal beam reflection for dual bands can be realized by employing a partition coding scheme. Taking the coding pattern depicted in Fig. 3(d) as an example, for *x*-polarized wave incidence, the phase gradient period Γ_1 = 3600 μm, resulting in a simulated abnormal reflection angle of approximately ±60.0° in the upper half of the metasurface at the optimal frequency of 95.5 GHz, as shown in Fig. 3(e). For *y*-polarized wave incidence, another coding sequence is applied; the phase gradient period Γ_2 = 7200 μm, and the corresponding abnormal reflection angle is about ±18.1° in the lower half of the metasurface at the optimal frequency of 134 GHz, as demonstrated in Fig. 3(f). Utilizing the partition coding scheme, independent beam manipulation of dual bands can be achieved at the same time.

Utilizing the 2D programmable capability of the proposed LCPM, single beamforming can be achieved. Fig. 4 presents the simulated and measured single-beam-scanning results of the LCPM with normalized gain. As shown in Figs. 4(a) and (b), for an *x*-polarized wave, the effective beam-scanning range in the *xoz* plane can reach ±50° (where the power gain of the reflection beam is reduced by no more than 5 dB), and the scanning angle in the *yoz* plane can cover the range of −50° to 10°. Figs. 4(c) and (d) demonstrate the corresponding measured results under identical conditions. Obviously, in the *xoz* plane, the single-beam-scanning angle can cover ±45° at the optimized operating frequency of 105 GHz. In the *yoz* plane, due to the blocking of the horn antenna, the scanning range is constrained to −40° to 10°. Far-field beam-scanning results at 103–110 GHz are also measured (Section S3 in Appendix A), showcasing the broadband coverage capability of the designed LCPM. The simulated single-beam-scanning results can be observed in the *xoz* and *yoz* planes under *y*-polarized wave incidence, as illustrated in Figs. 4(e) and (f). Furthermore, a comparison between the proposed LCPM and other related works on millimeter-wave and terahertz beam manipulation is provided in Table 1 [17,29,32–34,54,55]. Firstly, compared with programmable metasurfaces implemented with semiconductor devices or

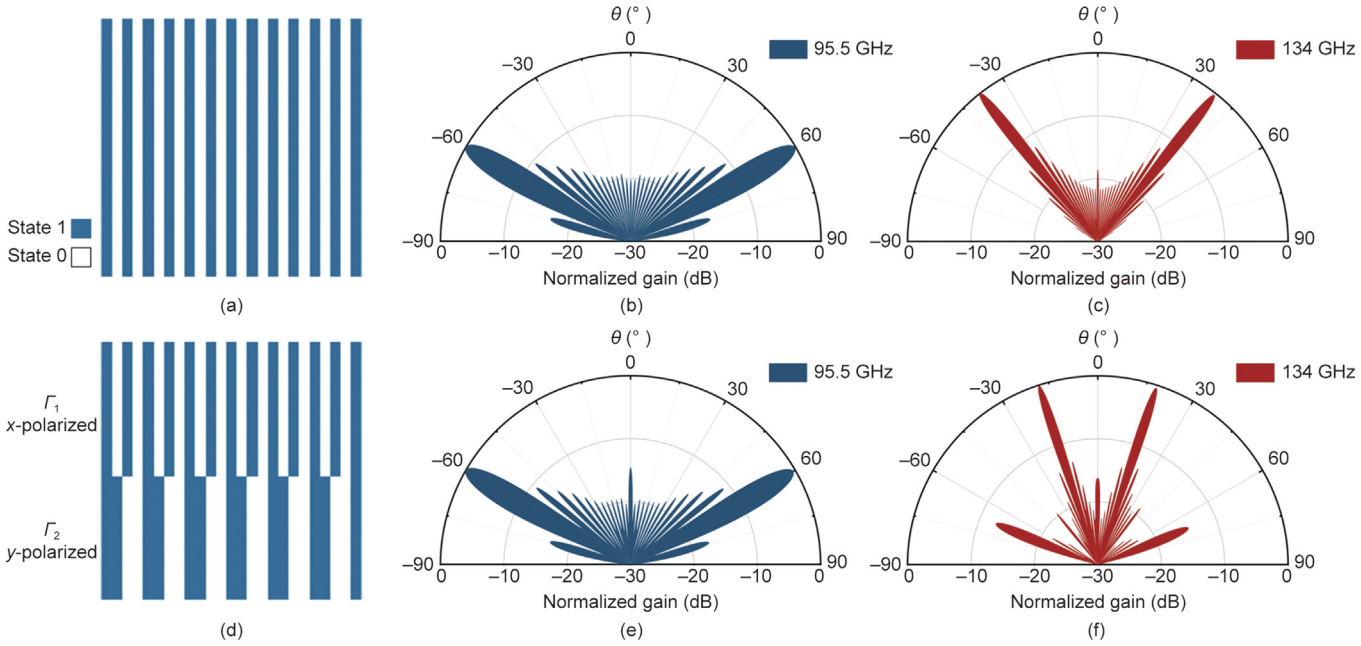

Fig. 3. The abnormal beam-reflection coding patterns and their corresponding simulated far-field pattern. (a) Abnormal reflection coding sequences of 10101010101010101010101. (b) The simulated far-field pattern at 95.5 GHz in the *yoz* plane for *x*-polarized plane wave incidence. (c) The simulated far-field pattern at 134 GHz in the *yoz* plane for *y*-polarized plane wave incidence. (d) The partition coding scheme: For *x*-polarized plane wave incidence, the coding sequence is 10101010101010101010101 in the upper half of the metasurface. For *y*-polarized plane wave incidence, the coding sequence is 110011001100110011001 in the lower half of the metasurface. (e) The simulated far-field pattern in the *yoz* plane at 95.5 GHz using the upper half of the metasurface for *x*-polarized plane wave incidence. (f) The simulated far-field pattern in the *yoz* plane at 134 GHz using the lower half of the metasurface for *y*-polarized plane wave incidence. Γ_1 and Γ_2: the phase gradient periods.

processes, the LC-based scheme offers significant cost advantages. Secondly, the demonstrated LCPM achieves excellent 2D beam scanning, covering 90° for *x*-polarized wave incidence and 60° for *y*-polarized wave incidence. The novel dual-band programmability of the LCPM further increases its application value. Additionally, the proposed LCPM supports a larger array scale while realizing 2D programmability.

The aforementioned results validate the proposed LCPM's ability to effectively manipulate terahertz waves across dual-broadband ranges and thereby offer substantial support for assisting wireless communications.

3. Materials and methods

3.1. Machining of the 1-bit LCPM

The top metal pattern with a thickness of 300 nm was etched on the bottom surface of a 200 μm-thick quartz substrate by means of a lithography process. Multilayer PCB manufacturing technology was used to process the pixel array of the metal feed structure. An LC layer with a thickness of 60 μm was filled between the quartz and PCB using a vacuum infusion process. The pixelated patch electrodes of the LCPM elements were interfaced with a DAC module, allowing for the independent application of a driven voltage to each element. In this work, the LCPM has 25 × 25 independently controllable super-elements. More details can be found in a previous work [56].

3.2. Far-field beam pattern simulation and measurement

In our simulation, the horn antenna was placed in the *yoz* plane, located at a 30° offset angle, and the distance between the phase center of the horn antenna and the LCPM was about 4.73 cm under *x*-polarized wave incidence. The corresponding far-field beam pattern measurement is shown in Section S3. Seven pieces of TI DAC60096 evaluation modulo board were used to realize independent control of each super-element in the LCPM. For *y*-polarized wave incidence, the horn antenna was placed above the center of the LCPM plane to illuminate the metasurface vertically, and the distance between the phase center of the horn antenna and the LCPM was about 6.02 cm in the simulation. Due to operating frequency limitations in the anechoic chamber, the far-field beam patterns under *y*-polarized wave incidence were not measured.

3.3. Terahertz wireless communication system

To verify the effectiveness of the LCPM in assisting terahertz wireless communications, a terahertz wireless communication system was constructed. In this system, both the Tx and Rx mainly consisted of a baseband processing unit based on a PXIe chassis and a radio frequency (RF) unit for up/down conversion of the electromagnetic waves. The Tx and Rx setups also included signal sources for local oscillation (LO) signal generation and rubidium (Rb) clocks to provide accurate frequency references and trigger signals to the LO sources and PXIe chassis. In the baseband processing unit of the Tx, the bit streams were first randomly generated and then coded using the Turbo scheme for error correction. Then, the coded bits were modulated using certain modulation schemes, such as QPSK and 64-QAM. The modulated symbols were carried on an orthogonal frequency-division multiplexing (OFDM) waveform. The OFDM waveform included eight component carriers, each with a 100 MHz bandwidth, and 1200 subcarriers with 75 kHz intervals. As for the time division scheme, a frame structure with a 10 ms duration was used, in which each frame contained 50 subframes and each subframe contained 14 OFDM symbols, resulting in a symbol rate of 153.6 megabits per second (Mbps). The OFDM symbols were converted into analog waveforms with DAC and up-converted to an

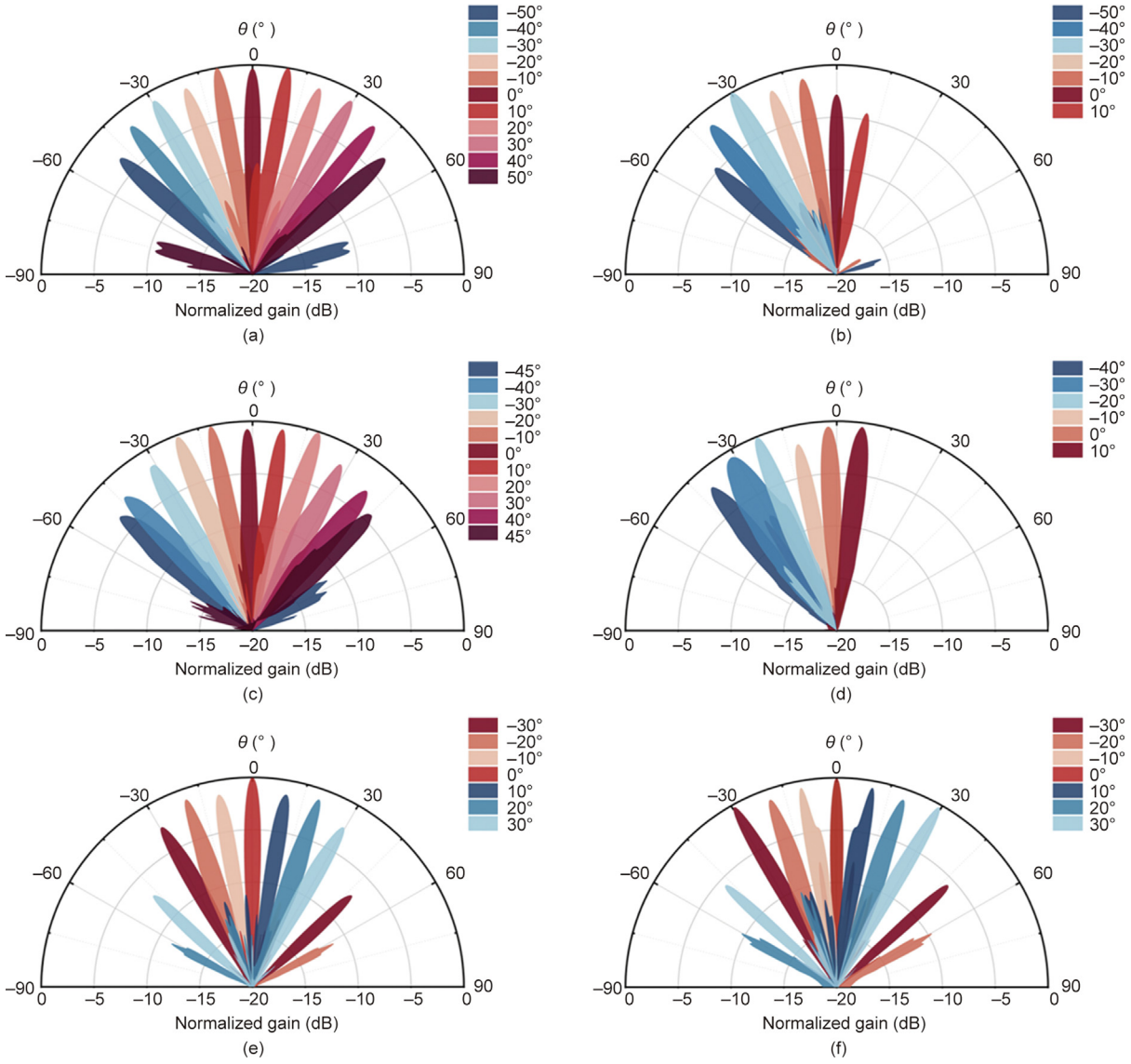

Fig. 4. Simulated and measured results of single beamforming under different polarized wave incidences. The normalized simulation results at 95.5 GHz under *x*-polarized wave incidence are presented in two planes: (a) the *xoz* plane and (b) the *yoz* plane. (c, d) Corresponding measured results at the optimized frequency of 105 GHz in (c) the *xoz* plane and (d) the *yoz* plane. (e, f) Normalized simulation results at 134 GHz under *y*-polarized wave incidence, presented in two planes: (e) the *xoz* plane and (f) the *yoz* plane.

Table 1
Comparison of related works on millimeter-wave and terahertz beam manipulation.

Ref.	Frequency (GHz)	Working polarization	Scanning dimension	Scanning range (°)	Array scale	Reconfiguration scheme	Fabrication cost
[17]	425	Single polarization	1D	42.8	90 × 48	VO_2	Low
[29]	340	Single polarization	1D	20–60	64 × 64	GaN HEMT	High
[32]	28.5	Dual polarization	2D	90	10 × 10	LC (30 μm)	Low
[33]	98	Dual polarization	1D	5–40	55 × 55	LC (80 μm)	Low
[34]	28	Four polarization	2D	100	10 × 10	LC (100 μm)	Low
[54]	110	Single polarization	1D	20–35	29 × 33	LC (40 μm)	Low
[55]	25	Single polarization	2D	140	30 × 30	PIN diode	High
This work	105	*x* polarization	2D	90	50 × 50	LC (60 μm)	Low
This work	134 (simulation)	*y* polarization	2D	60 (simulation)	50 × 50	LC (60 μm)	Low

intermediate frequency (IF) within the range of 8.5–13.5 GHz. The IF signal was further transmitted into the RF unit of the Tx and then mixed with a terahertz LO signal generated through digital signal generation and a 12-times multiplier. The modulated OFDM signal was then upconverted to the terahertz band and radiated out through the Tx antenna.

After the terahertz signal propagated through the wireless channels and interacted with the LCPM or other objects, it was captured at the Rx. Inversely, the received terahertz signal was down-converted to the IF by mixing it with an LO signal with the same frequency as that of the Tx LO signal. The IF signal was then transmitted to the PXIe chassis and further down-converted to

the baseband, which was further demodulated and decoded. Thus, corresponding constellation diagrams and error vector magnitude (EVM) values could be measured to evaluate the link performance. A gigabits per second (Gbps) real-time video demonstration could also be realized through the communication process described above. Detailed descriptions of the system hardware and software structures are provided in Appendix A Section S4.

4. Experimental verification of LCPM-assisted terahertz wireless communications

4.1. LCPM-aided terahertz wireless communications

For a certain terahertz link, the received signal at the Rx can be expressed as follows:

$$\boldsymbol{y} = \sqrt{P_{\mathrm{t}} G_{\mathrm{t}} G_{\mathrm{r}}} \left(\boldsymbol{\alpha}_{\mathrm{LoS}} \mathrm{e}^{-\mathrm{j}2\pi f \tau_{\mathrm{LoS}}} + \sum_{l=1}^{L} \boldsymbol{\alpha}_l \mathrm{e}^{-\mathrm{j}2\pi f \tau_l} \right) \tag{2}$$

where $\boldsymbol{y}$ is the received signal, P_{t} is the transmit power; G_{t} and G_{r} are the antenna gains of the Tx and Rx, respectively; and $\boldsymbol{\alpha}_{\mathrm{LoS}}$ and $\boldsymbol{\alpha}_l$ denote the complex path gains of the LoS path and the lth NLoS path ($1 \le l \le L$), respectively. L is the number of NLoS paths, and j represents the imaginary unit. Moreover, f is the carrier frequency, and τ_{LoS} and τ_l are the propagation delays of the LoS path and the lth NLoS path, respectively.

When the LoS path is absent, the NLoS paths are usually too weak to provide an effective link connection due to the large diffraction, reflection, and penetration losses in the terahertz band. As a result, the LCPM is applied to provide a stable and strong reflection path, where the received signal shows the following form:

$$\boldsymbol{y} = \sqrt{P_{\mathrm{t}} G_{\mathrm{t}} G_{\mathrm{r}}} \left(\boldsymbol{\alpha}_{\mathrm{Tx-LCPM-Rx}} \sum_{k=1}^{K} A_k \mathrm{e}^{-\mathrm{j}2\pi f \tau_k + \phi_k} \right) \tag{3}$$

where $\boldsymbol{\alpha}_{\mathrm{Tx-LCPM-Rx}}$ denotes the overall path gain of the LCPM-aided communication link; K presents the number of elements on the LCPM; and A_k and ϕ_k are the amplitude and phase responses of the kth ($1 \le k \le K$) element, respectively. Additionally, τ_k is the overall propagation delay from the Tx to the kth element on the LCPM and then to the Rx.

Under normal incidence from the Tx to the LCPM and far-field propagation, Eq. (3) can be further derived in the following form:

$$\boldsymbol{y}(\theta, \varphi) = \sqrt{P_{\mathrm{t}} G_{\mathrm{t}} G_{\mathrm{r}}} \left(\boldsymbol{\alpha}_{\mathrm{Tx-LCPM-Rx}} \mathrm{e}^{-\mathrm{j}2\pi f \tau_0} \sum_{m=1}^{M} \sum_{n=1}^{N} A_{m,n} \mathrm{e}^{-\mathrm{j}\left(\frac{2\pi}{\Phi}(m d_x \sin\theta \cos\varphi + n d_y \sin\theta \sin\varphi) + \phi(m,n)\right)} \right) \tag{4}$$

where τ_0 denotes the overall propagation delay from the Tx to the LCPM and then to the Rx, and $M \times N$ is the array scale of the LCPM. $A_{m,n}$ and $\phi(m,n)$ ($1 \le n \le N$, $1 \le m \le M$) represent the amplitude and phase of the (mth, nth) super-element, and d_x and d_y are the period lengths of the super-element in the x and y directions, respectively. Moreover, φ is the azimuth angle of the target wireless channel.

From Eq. (4), it can be seen that the communication link constructed by the aid of the LCPM depends on the complex composition of the signals reflected from each super-element; thus, it is highly controllable through changing the amplitude and phase responses on each super-element. For example, by applying either high or low voltage levels, the phase responses of the super-elements on the LCPM are either 0 or 180°, while the amplitude response remains unchanged. Therefore, with a certain coding pattern on the LCPM, the received signals on the super-elements can be constructively superposed in a certain direction while they are destructively superposed in other directions, creating a specific reflected beam. By changing the coding patterns on the LCPM, the beam direction can be correspondingly changed and adapted to user locations.

4.2. Communication link establishment and channel regulation verification

To illustrate the effectiveness of the proposed LCPM-aided terahertz communications, the terahertz wireless links were carefully assessed under different conditions, including an LoS link, an obstructed LoS (OLoS) link, a PRS-aided link, and an LCPM-aided link; the testing environment and results are demonstrated in Fig. 5. Notably, the overall propagation distance was kept constant at 1.15 m, and the carrier frequency was selected as 140 GHz. The overall propagation distance refers to the separation distance between the Tx and Rx under both LoS and OLoS conditions. Alternatively, it can be the summation of the distance from the Tx to the PRS/LCPM and that from the PRS/LCPM to the Rx. A digital modulation constellation diagram and EVM are used to evaluate the link quality. For a certain constellation point, the EVM is calculated as follows:

$$\mathrm{EVM\ (dB)} = 20 \log_{10} \frac{\min\limits_{j} |c_i^{\mathrm{M}} - c_j^{\mathrm{T}}|}{\max\limits_{j} |c_j^{\mathrm{T}}|} \tag{5}$$

where c_i^{M} is the ith measured complex constellation point and c_j^{T} is the jth true constellation point. i and j are positive integers. In Figs. 5(a) and (b), it is evident that the QPSK constellation diagram is extremely distinct under LoS propagation, with an EVM value of −22.5 dB. However, when the LoS path is blocked by objects, such as the door illustrated in Fig. 5(c), the communication link is interrupted and no signal can be received at the Rx, as demonstrated in Fig. 5(d).

To address this issue, both PRS and LCPM schemes are evaluated and compared. As can be seen in Fig. 5(e), when the PRS-aided link meets the specular reflection criterion—that is, the incident elevation angle from the Tx to the PRS matches the emergence elevation angle from the PRS to the Rx—the link performance closely resembles that of a direct LoS link, with a clear QPSK constellation diagram and an EVM value of −18.9 dB (Fig. 5(f)). However, meeting the specular reflection condition is typically challenging, given that users will move casually, while the position and orientation of the PRS is fixed. When non-specular scattering occurs on the PRS, the additional scattering loss will be significant, and the link performance is dramatically degraded. For instance, keeping the incident elevation angle θ_{i} at 45°, the EVM value is only −7.3 dB when the emergence elevation angle θ_{e} is 20°, as depicted in Fig. 5(g). In this case, the constellation diagram is barely distinguishable. Furthermore, setting θ_{e} to 5° renders the constellation diagram completely unrecognizable, leading to failure in the communication link, as demonstrated in Fig. 5(h).

In contrast, the terahertz wireless link supported by the LCPM is demonstrated in Fig. 5(i). The Tx illuminates vertically onto the LCPM, and the emergence elevation angle θ_{e} and azimuth angle φ_{e} of the wireless channel can be flexibly adjusted by altering the coding pattern of the LCPM to ensure a link connection between the Tx and Rx. In the following measurements, the column coding scheme is implemented to build the wireless communication link. First, φ_{e} is fixed to 180°, while θ_{e} varies from 15° to 55° by moving the Rx. The measured constellation diagrams and the corresponding EVM values are depicted in Figs. 5(j)–(l) and Figs. 5(o) and (p), respectively. As the Rx moves, the measured constellation diagrams remain distinguishable with excellent link quality, thereby validating the effectiveness of the LCPM in regulating the wireless channel. It should be noted that, as θ_{e} increases, the measured EVM value increases accordingly, indicating a deterioration in wireless channel quality. This can be attributed to the decrease in beam gain shaped by the LCPM that occurs as θ_{e} increases. Furthermore, a wireless link with θ_{e} = 38° and

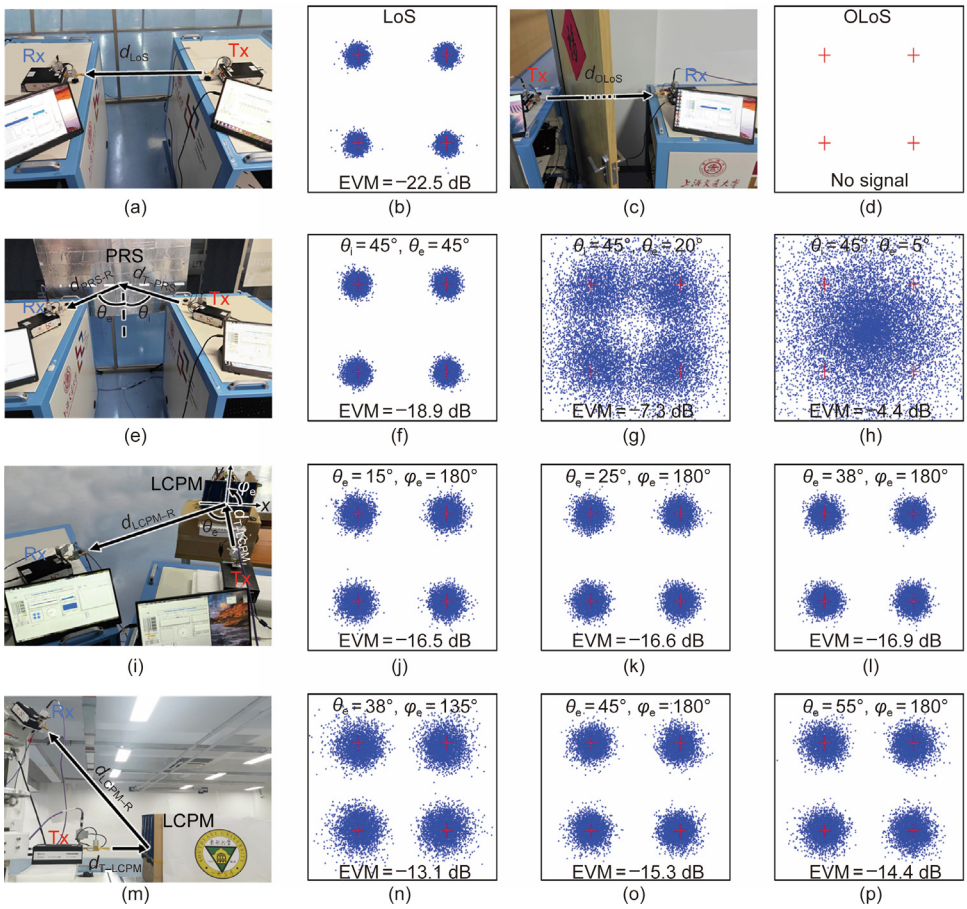

Fig. 5. Terahertz communication experiments and link performance results under different conditions. (a, b) A direct LoS link is tested with a distance d_{LoS} of 1.15 m. (c, d) The LoS link is blocked by a door, and the received signal is too weak to be received. Thus, no constellation diagram and EVM value are measured. The separation distance d_{OLoS} from the Tx to Rx is set as 1.15 m. (e–h) A PRS made of metal foils used to provide terahertz communication links under NLoS conditions. For illustration clearance, the blockage object is not shown. The distance from the Tx to PRS and that from the PRS to Rx are both set as 0.575 m. The PRS-aided terahertz links are tested with an incident elevation angle $\theta_i = 45°$ and an emergence elevation angle θ_e ranging from 5° to 45°. (i–l, o–p) The proposed LCPM is utilized to enable terahertz communication under NLoS conditions. Normal incidence from the Tx is set; that is, $\theta_i = 0°$. The emergence elevation angle θ_e ranges from 15° to 55°. The distance from the Tx to the LCPM is set as 0.15 m, and the distance from the LCPM to the Rx is set as 1.00 m. (m, n) Establishment of a wireless channel with $\theta_e = 38°$ and $\varphi_e = 135°$. The distance from the Tx to the LCPM is set as 0.15 m and the distance from the LCPM to the Rx is set as 1.00 m. φ_e: the azimuth angle; d_{LoS}: the distance from the Tx to Rx for LoS link; d_{OLoS}: the distance from the Tx to Rx for OLoS link; d_{T-PRS}: the distance from the Tx to the PRS; d_{PRS-R}: the distance from the PRS to the Rx; d_{T-LCPM}: the distance from the Tx to the LCPM; d_{LCPM-R}: the distance from the LCPM to the Rx.

$\varphi_e = 135°$ was established by exerting the 2D programmable capability of the LCPM, as illustrated in Fig. 5(m). The corresponding constellation diagram and EVM value are presented in Fig. 5(n). To assess the quality of the wireless channel provided by the LCPM under the condition of ($\theta_e = 38°$ and $\varphi_e = 135°$), which corresponds to the worst EVM value measured under different directions, the wireless video transmission in QPSK modulation can be stably demonstrated (see Video S1 in Appendix A for more details), indicating that effective link connection was realized.

To summarize, the experimental results indicate that a wireless channel can be effectively established and dynamically regulated by the LCPM under an NLoS scenario, facilitating stable terahertz wireless communications.

4.3. High-order and wideband communication measurements

Based on the wireless link created by the LCPM, high-order modulation schemes were further assessed. Fig. 6(a) illustrates the measured constellation diagram, along with the corresponding link performance, for 64-QAM modulation at a carrier frequency of 140 GHz. The test results clearly demonstrated that the terahertz wireless communication link established via the LCPM could accommodate communication modulation ranging from QPSK to 64-QAM at least. The measured link throughput reached 2474.8 Mb·s^{-1}, indicating that high-speed data transmission was supported. Furthermore, real-time video transmission under the 64-QAM modulation was carried out (see Video S1 for more details), as illustrated in Fig. 6(b).

To further evaluate the broadband characteristics of the LCPM, constellation diagrams and EVM values at different carrier frequencies from 135 to 145 GHz were tested and are presented here. Figs. 6(c)–(e) show the measured constellation diagrams for the 64-QAM modulation scheme at 135, 140, and 145 GHz, respectively. Distinguishable constellation diagrams can be observed, exhibiting the broadband capability of the LCPM in assisting terahertz wireless communication. More intuitively, Fig. 6(f) presents the EVM results across the 10 GHz wide band for 64-QAM modulation. It is apparent that the EVM values remain stable when the carrier frequency varies from 135 to 145 GHz. Compared with the EVM values under LoS transmission, those for LCPM-aided links are around 4 dB higher. This phenomenon arises because, apart from the self-loss introduced by the LCPM, nearly half of the energy is reflected in the opposite direction, as a symmetrical dual beam regulated by the 1-bit programmable metasurface under the

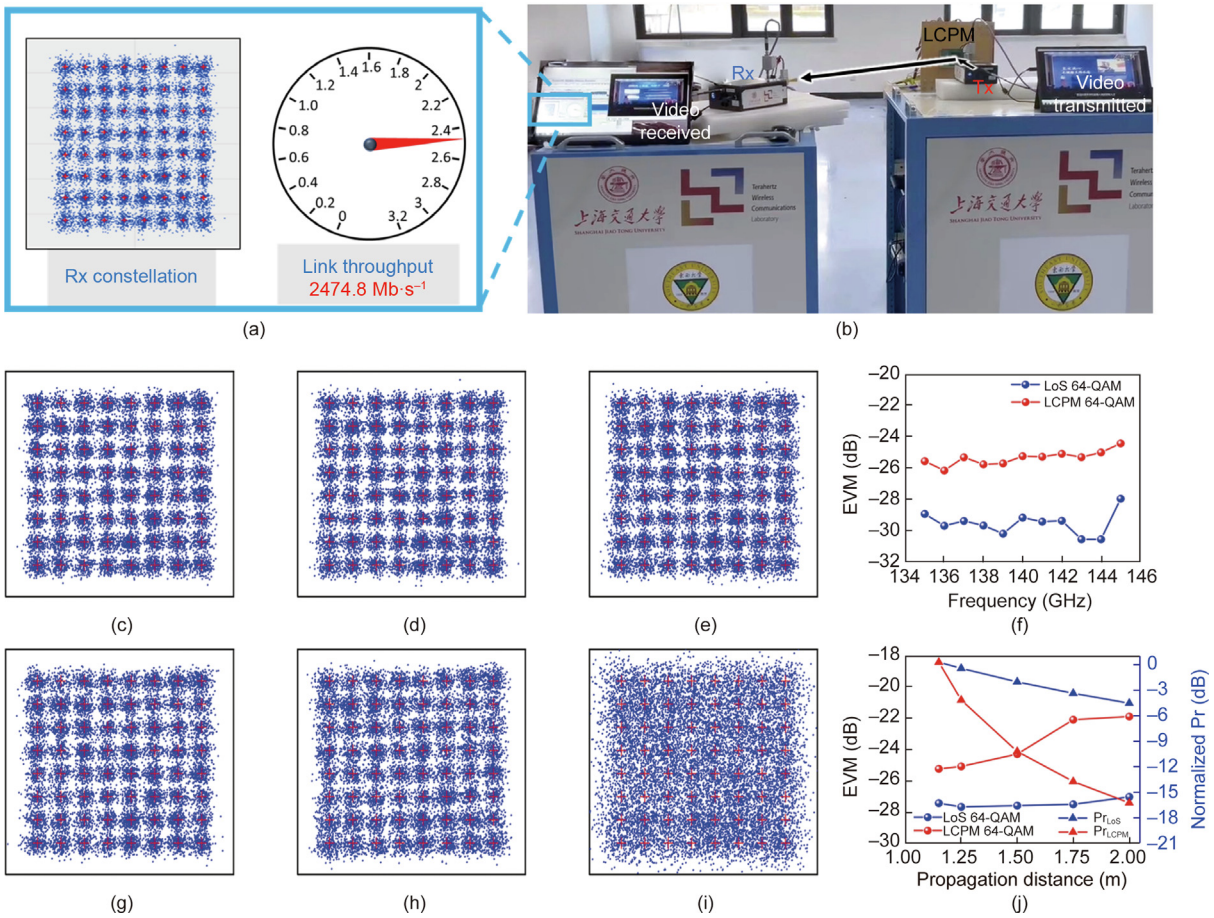

Fig. 6. Performance measurements of real-time video transmission and broadband and long-distance propagation under 64-QAM modulation. (a, b) Scenario of real-time video transmission under 64-QAM modulation, along with the measured link performance; the carrier frequency is 140 GHz, the propagation distance is 1.15 m, and θ_e = 38°. (c–e) 64-QAM modulation constellation diagrams at 135, 140, and 145 GHz. The propagation distance is 1.15 m, and θ_e = 38°. (f) Measured EVM values of LoS links and LCPM-aided links with different carrier frequencies; the propagation distance is 1.15 m, and θ_e = 38°. (g–i) 64-QAM modulation constellation diagrams at the carrier frequency of 140 GHz when the propagation distance is 1.25, 1.50, and 1.75 m, respectively. (j) Measured EVM values and calculated normalized received powers of LoS links and LCPM-aided links with different propagation distances; the carrier frequency is 140 GHz and θ_e = 38°. Pr: the received power; Pr_{LoS}: the received power at the Rx of LoS links; Pr_{LCPM}: the received power at the Rx of LCPM-aided links.

column coding scheme is inevitable. Increasing the number of phase quantization bits can suppress the energy loss caused by symmetrical beams, further improving the quality of the wireless channel (Section S5 in Appendix A).

Subsequently, the link performance under different propagation distances was assessed at 140 GHz. Variation of the propagation distance was accomplished by changing the distance between the Tx and LCPM from 0.15 to 1.00 m, while maintaining a constant distance of 1.00 m between the LCPM and Rx. Figs. 6(g)–(i) depict the constellation diagrams measured at overall propagation distances of 1.25, 1.50, and 1.75 m, respectively. As the propagation distance increases from 1.15 to 1.50 m, the constellation diagram remains clear, indicating that high-quality transmission can be realized across a long distance. Furthermore, when the propagation distance reaches 1.75 m, the constellation diagram becomes blurred, indicating significant deterioration in the link quality. For comparison, the EVM values at various propagation distances under the LoS condition were also measured, as shown in Fig. 6(j). In the LoS case, as the propagation distance increases from 1.15 to 2.00 m, the measured EVM values stabilize around −27.6 dB. However, for the LCPM-aided links, the measured EVM values change significantly with varying distances, which can be ascribed to the rapid decline of received power at the Rx when the distance between the Tx and LCPM increases. A detailed analysis is provided in Section 5.

These experimental results indicate that the LCPM can effectively support long-distance and high-speed wireless communications in an NLoS scenario. Additionally, the working bandwidth of over 10 GHz reveals the broadband advantage of the LCPM in assisting terahertz wireless communications.

Experiments in LCPM-aided wireless communications were further conducted in the W band. The experimental scene is illustrated in Fig. 7(a): A normal incidence excitation mode is adopted, and the distance from the Tx to LCPM is set as 0.30 m. The distance from the LCPM to Rx is set as 1.00 m, and the carrier frequency is 105 GHz. The column coding scheme was applied in the following tests. Figs. 7(b)–(d) present the measured constellation diagrams and the corresponding EVM values at different emergence elevation angles under the QPSK modulation. Similar to the results demonstrated in the D band, the LCPM exhibits excellent dynamic channel regulation ability. When θ_e = 40°, various modulation schemes including QPSK, 16-QAM, and 64-QAM were verified, as shown in Figs. 7(d)–(f). Distinguishable constellation diagrams were obtained at the Rx, indicating the excellent link quality of the LCPM-aided terahertz communications. In the frequency range from 103 to 110 GHz, the broadband feature was validated through single-beam scanning (Section S3). Furthermore, Figs. 7(g)–(i) illustrate the constellation diagrams and EVM values measured at different propagation distances of 1.30, 1.80, and 2.30 m, respectively, when θ_e = 52°, reconfirming the capability

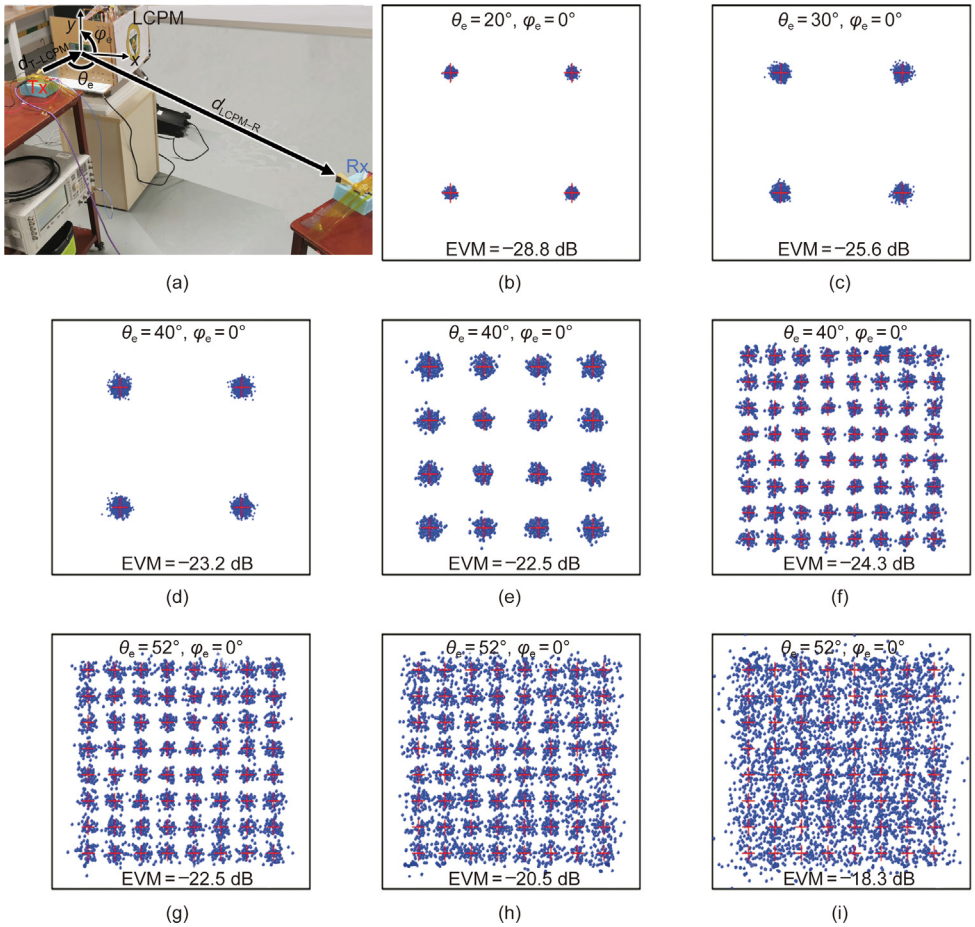

Fig. 7. LCPM-aided wireless communications in an NLoS scene at the W band and the corresponding measured results. (a) The LCPM-aided wireless communications system, in which the normal incidence from the Tx is set, that is, $\theta_i = 0$. The emergence elevation angle θ_e ranges from 20° to 52°. The distance from the Tx to LCPM is set as 0.30 m, and the distance from the LCPM to Rx is set as 1.00 m. (b–d) Measured constellation diagrams and EVM values at different emergence elevation angles for the QPSK modulation. (e, f) Measured constellation diagrams and EVM values corresponding to 16-QAM and 64-QAM modulations at θ_e = 40°. (g–i) 64-QAM modulation constellation diagrams when the propagation distance is 1.30, 1.80, and 2.30 m, respectively. Variation in the propagation distance is achieved by changing the distance from the Rx to the LCPM.

of long-distance transmission. It should be noted that different hardware systems were used to conduct the communication experiments in the two different bands, which resulted in differences in the measured constellation diagrams and EVM values.

In summary, our experiments substantiate the ability of the LCPM to assist dual-broadband and long-distance terahertz high-speed wireless communications.

5. Discussion and conclusions

In Fig. 6(j), the measured EVM values of the LCPM-aided links deteriorate more rapidly than those of the LoS link when the propagation distance increases from 1.15 to 1.75 m. The reason is discussed as follows. Under LoS transmission conditions, the relationship between the received power (Pr_{LoS}) at the Rx and the propagation distance can be expressed as follows:

$$Pr_{LoS} \propto \frac{1}{d_{LoS}^2} \tag{6}$$

where d_{LoS} denotes the distance from the Tx to Rx. For the LCPM-aided link, the received power (Pr_{LCPM}) at the Rx is influenced by both the distance between the Tx and LCPM and the distance between the LCPM and Rx [57]. In our measurements, only the distance from the Tx to LCPM was changed to realize variation in the total propagation distance. Consequently, the relationship between Pr_{LCPM} and the distance from the Tx to LCPM can be simplified as follows:

$$Pr_{LCPM} \propto \frac{1}{d_{T-LCPM}^2} \tag{7}$$

where d_{T-LCPM} is the distance from the Tx to LCPM. Accordingly, the variation in the received power with respect to the propagation distance can be calculated, as demonstrated in Fig. 6(j). For an intuitive comparison, we normalize both Pr_{LoS} and Pr_{LCPM} to 0 dB at a propagation distance of 1.15 m. Based on Eq. (6), as the propagation distance varies from 1.15 to 1.75 m, the corresponding Pr_{LoS} drops by approximately 3.6 dB, with a slight impact on the wireless channel. However, for the NLoS transmission, the Pr_{LCPM} calculated by Eq. (7) decreases by about 14.0 dB when the propagation distance increases from 1.15 to 1.75 m, resulting in a significant deterioration in the measured EVM values.

To summarize, we have proposed a novel dual-broadband LCPM capable of flexibly manipulating terahertz waves and effectively assisting terahertz wireless communications in NLoS transmission scenarios. The LCPM's powerful beam-control capabilities—which include dual beam steering, single-beam scanning, and dual-band independent beam regulation based on a partition coding scheme—lay a solid foundation for assisting in terahertz wireless communications. The establishment and flexible regulation of wireless channels were demonstrated in 3D space utilizing the

pixel-level programmable capability of the LCPM, verifying the feasibility of using the LCPM to aid terahertz wireless communications. The wireless link provided by the LCPM can support QPSK, 16-QAM, and 64-QAM modulation communications with a long propagation distance. Furthermore, real-time video transmission was showcased across various modulation schemes, confirming the effectiveness and stability of the wireless channel created by the LCPM. The stable channel connection over a broad frequency range enables ultra-wideband and ultra-high-speed data transmissions, satisfying the demands of 6G wireless communication networks.

Inspired by the above research, the next step will focus on improving the phase coding from 1-bit to 2-bit and beyond to achieve more effective beam manipulation. In addition, reducing the thickness of the LC to increase the device's response speed will be important in order to better satisfy the demands of future wireless communication scenarios. Finally, the results of this work primarily validate the feasibility and efficacy of the proposed LCPM in aiding terahertz wireless communications. The development of an intelligent LCPM that integrates sensing and communications will be a key exploration direction in future efforts.

CRediT authorship contribution statement

Yuan Fu: Writing – original draft, Validation, Methodology, Investigation, Conceptualization. **Yuanbo Li:** Writing – original draft, Validation, Investigation. **Xiaojian Fu:** Writing – review & editing, Validation, Supervision, Conceptualization. **Lu Xu:** Validation. **Yujie Liu:** Validation. **Qun Yan Zhou:** Validation. **Jun Yang:** Validation. **Chong Han:** Writing – review & editing, Validation, Supervision. **Jun Yan Dai:** Validation. **Qiang Cheng:** Validation. **Tie Jun Cui:** Writing – review & editing, Supervision, Conceptualization.

Declaration of competing interest

The authors declare that they have no known competing financial interests or personal relationships that could have appeared to influence the work reported in this paper.

Acknowledgments

This work was supported by the National Natural Science Foundation of China (U23A20279 and 62288101) and 111 Project (111-2-05). The authors would also like to thank Liu Cao, Lifeng Chen, Hang Xu, and Lihao Huang for their support in experimental measurements.

Appendix A. Supplementary data

Supplementary data to this article can be found online at https://doi.org/10.1016/j.eng.2025.08.040.

References

[1] Tonouchi M. Cutting-edge terahertz technology. Nat Photonics 2007;1(2):97–105.
[2] Nagatsuma T, Ducournau G, Renaud CC. Advances in terahertz communications accelerated by photonics. Nat Photonics 2016;10(6):371–9.
[3] Capmany J, Novak D. Microwave photonics combines two worlds. Nat Photonics 2007;1(6):319–30.
[4] Koenig S, Lopez-Diaz D, Antes J, Boes F, Henneberger R, Leuther A, et al. Wireless sub-THz communication system with high data rate. Nat Photonics 2013;7(12):977–81.
[5] Akyildiz IF, Jornet JM, Han C. Terahertz band: next frontier for wireless communications. Phys Commun 2014;12(9):16–32.
[6] Dang S, Amin O, Shihada B, Alouini MS. What should 6G be? Nat Electron 2020;3(1):20–9.
[7] Wang CX, You X, Gao X, Zhu X, Li Z, Zhang C, et al. On the road to 6G: visions, requirements, key technologies, and testbeds. IEEE Commun Surv Tutor 2023;25(2):905–74.
[8] Akyildiz IF, Han C, Hu ZF, Nie S, Jornet JM. Terahertz band communication: an old problem revisited and research directions for the next decade. IEEE Trans Commun 2022;70(6):4250–85.
[9] Han C, Bicen AO, Akyildiz IF. Multi-ray channel modeling and wideband characterization for wireless communications in the terahertz band. IEEE Trans Wirel Commun 2015;14(5):2402–12.
[10] Jacob M, Priebe S, Dickhoff R, Kleine-Ostmann T, Schrader T, Kurner T. Diffraction in mm and sub-mm wave indoor propagation channels. IEEE Trans Microw Theory Tech 2012;60(3):833–44.
[11] Han C, Li Y, Wang Y, Yu Z. Still waters run deep: extend THz coverage with non-intelligent reflecting surface. IEEE Wirel Commun 2024;31(1):41–7.
[12] Li Y, Wang Y, Chen Y, Yu Z, Han C. Channel measurement and coverage analysis for NIRS-aided THz communications in indoor environments. IEEE Commun Lett 2023;27(9):2486–90.
[13] Ju S, Shakya D, Poddar H, Xing YC, Kanhere O, Rappaport TS. 142 GHz sub-terahertz radio propagation measurements and channel characterization in factory buildings. IEEE Trans Wirel Commun 2024;23(7):7127–43.
[14] Hu S, Rusek F, Edfors O. Beyond massive MIMO: the potential of data transmission with large intelligent surfaces. IEEE Trans Signal Process 2018;66(10):2746–58.
[15] Li L, Shuang Y, Ma Q, Li H, Zhao H, Wei M, et al. Intelligent metasurface imager and recognizer. Light Sci Appl 2019;8(10):97.
[16] Li L, Zhao H, Liu C, Li L, Cui TJ. Intelligent metasurfaces: control, communication and computing. eLight 2022;2:7.
[17] Chen B, Wang X, Li W, Li C, Wang ZS, Guo H, et al. Electrically addressable integrated intelligent terahertz metasurface. Sci Adv 2022;8(41):eadd1296.
[18] Cui TJ, Qi MQ, Wan X, Zhao J, Cheng Q. Coding metamaterials, digital metamaterials and programmable metamaterials. Light Sci Appl 2014;3(10):e218.
[19] Liu S, Noor A, Du LL, Zhang L, Xu Q, Luan K, et al. Anomalous refraction and nondiffractive Bessel-beam generation of terahertz waves through transmission-type coding metasurfaces. ACS Photonics 2016;3(10):1968–77.
[20] Zhuang X, Zhang W, Wang K, Gu Y, An Y, Zhang X, et al. Active terahertz beam steering based on mechanical deformation of liquid crystal elastomer metasurface. Light Sci Appl 2023;12(1):14.
[21] Grady NK, Heyes JE, Chowdhury DR, Zeng Y, Reiten MT, Azad AK, et al. Terahertz metamaterials for linear polarization conversion and anomalous refraction. Science 2013;340(6138):1304–7.
[22] Xiong B, Xu Y, Wang J, Li L, Deng L, Cheng F, et al. Realizing colorful holographic mimicry by metasurfaces. Adv Mater 2021;33(21):2005864.
[23] Yang W, Qin J, Long J, Yan W, Yang Y, Li C, et al. A self-biased non-reciprocal magnetic metasurface for bidirectional phase modulation. Nat Electron 2023;6(3):225–34.
[24] Liu Y, Wang Y, Fu X, Shi L, Yang F, Luo J, et al. Toward sub-terahertz: space–time coding metasurface transmitter for wideband wireless communications. Adv Sci 2023;10(29):2304278.
[25] Zhang L, Chen MZ, Tang W, Dai JY, Miao L, Zhou XY, et al. A wireless communication scheme based on space- and frequency-division multiplexing using digital metasurfaces. Nat Electron 2021;4(3):218–27.
[26] Yang Y, Wang W, Moitra P, Kravchenko II, Briggs DP, Valentine J. Dielectric meta-reflectarray for broadband linear polarization conversion and optical vortex generation. Nano Lett 2014;14(3):1394–9.
[27] Wang E, Peng G, Zhong K, Wu F, Jiang Z, Sauleau R, et al. A 1296-cell reconfigurable reflect-array antenna with 2-bit phase resolution for Ka-band applications. IEEE Trans Antenn Propag 2024;72(4):3425–37.
[28] Liang JC, Cheng Q, Gao Y, Xiao C, Gao S, Zhang L, et al. An angle-insensitive 3-bit reconfigurable intelligent surface. IEEE Trans Antenn Propag 2022;70(10):8798–808.
[29] Lan F, Wang L, Zeng H, Liang S, Song T, Liu W, et al. Real-time programmable metasurface for terahertz multifunctional wave front engineering. Light Sci Appl 2023;12(8):191.
[30] Kossifos KM, Georgiou J, Antoniades MA. ASIC-enabled programmable metasurfaces—part 1: design and characterization. IEEE Trans Antennas Propag 2024;72(3):2790–9.
[31] Kim H, Oh S, Bang S, Yang H, Kim B, Oh J. Independently polarization manipulable liquid-crystal-based reflective metasurface for 5G reflectarray and reconfigurable intelligent surface. IEEE Trans Antennas Propag 2023;71(8):6606–16.
[32] Aghabeyki P, Cai Y, Deng G, Tan ZH, Zhang S. A dual-polarized reconfigurable reflectarray with a thin liquid crystal layer and 2-D beam scanning. IEEE Trans Antennas Propag 2023;71(4):3282–93.
[33] Guirado R, Perez-Palomino G, De La Rosa P, Carrasco E, Quintana X. Electronically reconfigurable reflectarray antenna based on single-layer liquid crystal with independent dual-polarization control. IEEE Trans Antennas Propag 2024;72(7):5626–36.
[34] Aghabeyki P, Cai Y, Deng G, Frølund Pedersen G, Zhang S. Beam-scanning reflectarray with switchable polarization based on liquid crystal at millimeter wave. IEEE Trans Antennas Propag 2025;73(3):1894–9.
[35] Guo G, Zhang X, Niu L, Wu T, Chen X, Xu Q, et al. Programmable graphene metasurface for terahertz propagation control based on electromagnetically induced transparency. Carbon 2023;208(5):345–54.

[36] Chen B, Wu J, Li L, Zhang C, Fan K, Xue Q, et al. Programmable terahertz metamaterials with non-volatile memory. Laser Photonics Rev 2022;16(4):2100472.
[37] Zhang S, Chen X, Liu K, Li H, Xu Y, Jiang X, et al. Nonvolatile reconfigurable terahertz wave modulator. PhotoniX 2022;3(1):7.
[38] Wu J, Shen Z, Ge S, Chen B, Shen Z, Wang T, et al. Liquid crystal programmable metasurface for terahertz beam steering. Appl Phys Lett 2020;116(13):131104.
[39] Fu X, Shi L, Yang J, Fu Y, Liu C, Wu JW, et al. Flexible terahertz beam manipulations based on liquid-crystal-integrated programmable metasurfaces. ACS Appl Mater Interfaces 2022;14(19):22287–94.
[40] Li W, Chen B, Hu X, Guo H, Wang S, Wu J, et al. Modulo-addition operation enables terahertz programmable metasurface for high-resolution two-dimensional beam steering. Sci Adv 2023;9(42):eadi7565.
[41] Wang P, Fu X, Yang J, Fu Y, Cai Q, Liu Y, et al. Efficient manipulation of near-field terahertz waves: individually addressable transmissive meta-device. Laser Photonics Rev 2024;18(12):2400617.
[42] Malik BT, Khan S, Koziel S. Design and implementation of multi-band reflectarray metasurface for 5G millimeter wave coverage enhancement. Sci Rep 2024;14:15286.
[43] Shah ST, Shawky MA, Kazim JUR, Taha A, Ansari S, Hasan SF, et al. Coded environments: data-driven indoor localisation with reconfigurable intelligent surfaces. Commun Eng 2024;3(5):66.
[44] Tang J, Cui M, Xu S, Dai L, Yang F, Li M. Transmissive RIS for B5G communications: design, prototyping, and experimental demonstrations. IEEE Trans Commun 2023;71(11):6605–15.
[45] Pei X, Yin H, Tan L, Cao L, Li Z, Wang K, et al. RIS-aided wireless communications: prototyping, adaptive beamforming, and indoor/outdoor field trials. IEEE Trans Commun 2021;69(12):8627–40.
[46] Zhao Y, Feng Y, Ismail AM, Wang Z, Guan Y, Guo Y, et al. 2-bit RIS prototyping enhancing rapid-response space–time wavefront manipulation for wireless communication: experimental studies. IEEE Open J Commun Soc 2024;5(8):4885–901.
[47] Dai L, Wang BC, Wang M, Yang X, Tan J, Bi S, et al. Reconfigurable intelligent surface-based wireless communications: antenna design, prototyping, and experimental results. IEEE Access 2020;8(3):45913–23.
[48] Huo Y, Dong X, Ferdinand N. Distributed reconfigurable intelligent surfaces for energy-efficient indoor terahertz wireless communications. IEEE Internet Things J 2023;10(3):2728–42.
[49] Huang C, Yang Z, Alexandropoulos G, Xiong K, Wei L, Yuen C, et al. Multi-hop RIS-empowered terahertz communications: a DRL-based hybrid beamforming design. IEEE J Sel Areas Commun 2021;39(6):1663–77.
[50] An J, Yuen C, Xu C, Li H, Ng DWK, Di Renzo M, et al. Stacked intelligent metasurface-aided MIMO transceiver design. IEEE Wirel Commun 2024;31(4):123–31.
[51] An J, Yuen C, Guan Y, Di Renzo M, Debbah M, Poor HV, et al. Two-dimensional direction-of-arrival estimation using stacked intelligent metasurfaces. IEEE J Sel Areas Commun 2024;42(10):2786–802.
[52] Zhang Y, Wu Z, Xia J, Wu J, Yang K, Dong C, et al. Infrared metasurface absorber based on silicon-based CMOS process. Opt Express 2022;30(18):32937–47.
[53] Chang X, Pivnenko M, Shrestha P, Wu W, Zhang W, Chu D. Electrically tuned active metasurface towards metasurface-integrated liquid crystal on silicon (meta-LCoS) devices. Opt Express 2023;31(4):5378–87.
[54] Pérez-Quintana D, Aguirre E, Olariaga E, Kuznetsov SA, Lapanik VI, Sutormin VS, et al. Reconfigurable millimeter-wave reflectarray based on low-loss liquid crystals. IEEE Trans Antennas Propag 2024;72(1):531–41.
[55] Zhang JW, Qi ZJ, Wu LJ, Zhou QY, Dai JY, Cao WW, et al. A smart millimeter-wave base station for 6G application based on programmable metasurface. Natl Sci Rev 2025;12(4):nwaf017.
[56] Fu Y, Fu X, Yang S, Peng S, Wang P, Liu Y, et al. Two-dimensional terahertz beam manipulations based on liquid-crystal-assisted programmable metasurface. Appl Phys Lett 2023;123(11):111703.
[57] Tang W, Chen MZ, Chen X, Dai JY, Han Y, Di Renzo M, et al. Wireless communications with reconfigurable intelligent surface: path loss modeling and experimental measurement. IEEE Trans Wirel Commun 2021;20(1):421–39.